



Observing Carbon and Oxygen Carriers in Protoplanetary Disks at Mid-infrared Wavelengths

Dana E. Anderson^{1,7} , Geoffrey A. Blake² , L. Ilseadore Cleeves¹ , Edwin A. Bergin³ , Ke Zhang⁴ ,
Kamber R. Schwarz^{5,8} , Colette Salyk⁶ , and Arthur D. Bosman³ 

¹ Department of Astronomy, University of Virginia, 530 McCormick Road, Charlottesville, VA 22904, USA; da4vn@virginia.edu

² Division of Geological and Planetary Sciences, California Institute of Technology, 1200 East California Boulevard, Pasadena, CA 91125, USA

³ Department of Astronomy, University of Michigan, 1085 South University, Ann Arbor, MI 48109, USA

⁴ Department of Astronomy, University of Wisconsin–Madison, 475 North Charter Street, Madison, WI 53706, USA

⁵ Lunar and Planetary Laboratory, The University of Arizona, 1629 East University Boulevard, Tucson, AZ 85721, USA

⁶ Department of Physics and Astronomy, Vassar College, 124 Raymond Avenue, Poughkeepsie, NY 12604, USA

Received 2020 November 7; revised 2021 January 4; accepted 2021 January 6; published 2021 March 4

Abstract

Infrared observations probe the warm gas in the inner regions of planet-forming disks around young Sun-like T Tauri stars. In these systems, H₂O, OH, CO, CO₂, C₂H₂, and HCN have been widely observed. However, the potentially abundant carbon carrier CH₄ remains largely unconstrained. The James Webb Space Telescope (JWST) will be able to characterize mid-infrared fluxes of CH₄ along with several other carriers of carbon and oxygen. In anticipation of the JWST mission, we model the physical and chemical structure of a T Tauri disk to predict the abundances and mid-infrared fluxes of observable molecules. A range of compositional scenarios are explored involving the destruction of refractory carbon materials and alterations to the total elemental (volatile and refractory) C/O ratio. Photon-driven chemistry in the inner disk surface layers largely destroys the initial carbon and oxygen carriers. This causes models with the same physical structure and C/O ratio to have similar steady-state surface compositions, regardless of the initial chemical abundances. Initial disk compositions are better preserved in the shielded inner disk midplane. The degree of similarity between the surface and midplane compositions in the inner disk will depend on the characteristics of vertical mixing at these radii. Our modeled fluxes of observable molecules respond sensitively to changes in the disk gas temperature, inner radius, and total elemental C/O ratio. As a result, mid-infrared observations of disks will be useful probes of these fundamental disk parameters, including the C/O ratio, which can be compared to values determined for planetary atmospheres.

Unified Astronomy Thesaurus concepts: [Astrochemistry \(75\)](#); [Protoplanetary disks \(1300\)](#)

1. Introduction

(Exo)planetary studies are revealing the chemical composition of planets in our galaxy. Making chemical connections between planets and protoplanetary disks may help us determine the conditions under which these planets formed (e.g., Cridland et al. 2016). One promising method of comparison is through measuring elemental abundances, including the ratios of O/H, C/H, and C/O (e.g., Öberg et al. 2011; Madhusudhan 2019). Investigation of the elemental composition of gas in the inner regions of protoplanetary disks, up to a few astronomical units from the central star, is of particular interest because this region is thought to be representative of the terrestrial planet-forming environment in our own solar system.

Gas in the inner disk is mainly observed at near-to-mid-infrared wavelengths. Various carbon and oxygen carriers are observable in this range. The Spitzer Space Telescope has widely detected H₂O, CO₂, HCN, C₂H₂, and OH in T Tauri disks (e.g., Carr & Najita 2008; Pontoppidan et al. 2010; Carr & Najita 2011; Salyk et al. 2011; Pascucci et al. 2013). With Keck-NIRSPEC, the ν_3 band of CH₄ at around 3.3 μ m was found in absorption for the disk of T Tauri star GV Tau N (Gibb & Horne 2013). The high excitation temperatures derived for these molecules suggest that they are present in the warm inner regions of disks, consistent with the radii associated with terrestrial planet formation.

In addition to the volatile carriers, a significant source of carbon may be present in solid, refractory form. About half of the total carbon in the interstellar medium exists in a refractory phase (e.g., Savage & Sembach 1996; Mishra & Li 2015). Based on the lack of carbon found in primitive meteorites, roughly 90%–99% of the interstellar refractory carbon is expected to be released into the gas prior to planetesimal formation (Bergin et al. 2015). Various mechanisms have been proposed for the breakdown of refractory carbon in the protostellar and/or protoplanetary disk stages (Bauer et al. 1997; Finocchi et al. 1997; Gail 2001, 2002; Lee et al. 2010; Gail & Tieloff 2017; Anderson et al. 2017; van't Hoff et al. 2020). Evidence of the release of refractory carbon may be revealed through observations of carbon-bearing species in the disk gas and result in larger C/O ratios (Wei et al. 2019).

Here we present theoretical models investigating how well emission of observable molecules including, H₂O, OH, CO₂, C₂H₂, HCN, and CH₄, responds to changes in the major carbon and oxygen carriers in the inner regions of protoplanetary disks. The aim of this work is to understand if we can ascertain both the chemical history and bulk composition of the inner disk via near-to-mid-infrared observations, such as those anticipated by the upcoming James Webb Space Telescope (JWST). We explore several different chemical scenarios to determine how the fluxes of observable species are affected.

The paper is organized as follows. Section 2 describes modeling of the protoplanetary disk structure and chemistry. The resulting disk compositions, including a comparison of the

⁷ Virginia Initiative on Cosmic Origins Fellow.

⁸ Sagan Fellow.

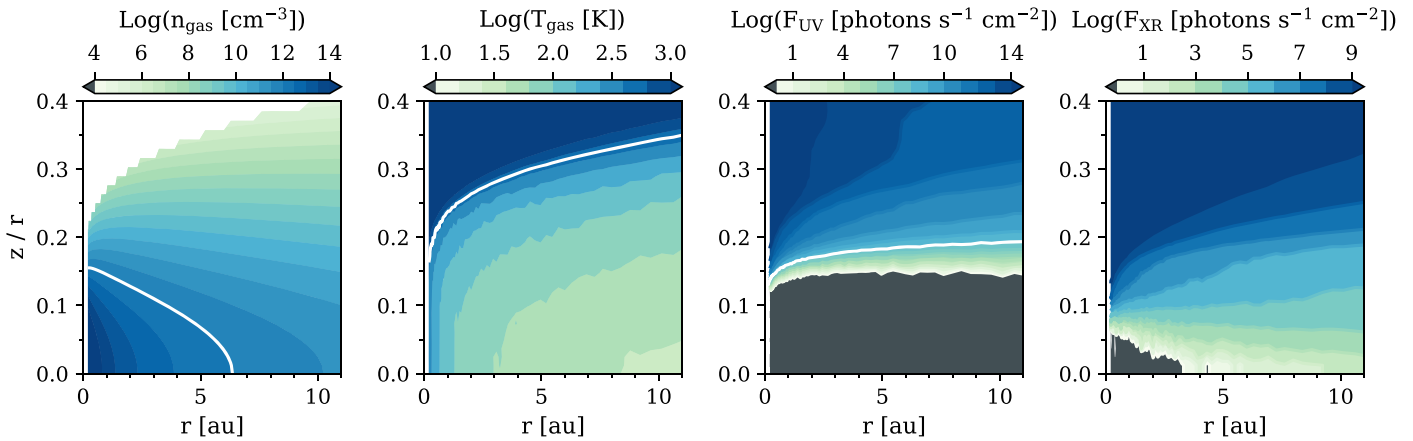


Figure 1. Physical structure of the modeled fiducial disk including the gas density, gas temperature, and UV continuum and X-ray radiation fields. Contours indicate the values of 10^{12} cm^{-3} , 500 K, and G_0 (Habing 1968) for reference.

observable surface column to the midplane, and the flux predictions for observable chemical species at mid-infrared wavelengths are presented in Section 3. The implications of our results are discussed in Section 4, followed by a summary of our main conclusions in Section 5.

2. Disk Modeling

2.1. Physical Structure

Our modeled disk surrounds a $1 M_{\odot}$ T Tauri star with a radius of $2.8 R_{\odot}$ and an effective temperature of 4300 K. Our fiducial disk model is azimuthally symmetric and has an outer radius of 120 au and a total gas mass of $0.01 M_{\odot}$. Two populations of dust composed of 80% astronomical silicates and 20% graphite (Draine & Lee 1984) are included. Each population follows a Mathis–Rumpl–Nordsieck (MRN) size distribution (Mathis et al. 1977). The large dust population has a maximum size of 1 mm and contains 90% of the total dust mass. The remaining dust mass exists in the small dust population, with a maximum size of $1 \mu\text{m}$. The minimum dust size for both populations is $0.005 \mu\text{m}$. The dust size distribution is used only in the temperature calculation and the UV and X-ray field calculations. Note that because the opacity coefficient κ is defined per unit dust mass, these disk properties are more sensitive to the maximum dust size for each population. The spatial distribution of the disk gas and dust follows that of Lynden-Bell & Pringle (1974); see also Andrews et al. (2011). A power law with an exponential cutoff,

$$\Sigma_{\text{gas}}(R) = \Sigma_c (R/R_c)^{-1} \exp[-(R/R_c)], \quad (1)$$

where $\Sigma_c = 23.0 \text{ g cm}^{-2}$ and $R_c = 30 \text{ au}$, describes the fixed radial surface density distribution of gas. For simplicity, the dust surface densities are assumed to have the same structure with $100\times$ lower Σ_c . The surface density is chosen to normalize the total disk mass to $0.01 M_{\odot}$, which is close to the minimum-mass solar nebula. The scale height of both the gas and the small dust population is 10 au at a radius of 100 au and distributed radially with a power law of $H/R \propto R^{0.15}$. The scale height of the large dust population is $5\times$ lower in order to approximate dust settling. This results in a gas-to-dust ratio of 1000 in the surface layers where only small dust resides, while the vertically integrated gas-to-dust ratio is 100.

The disk is passively heated by the central star, and dust temperatures are calculated using TORUS (Harries et al. 2004). The Monte Carlo radiative transfer code of Bethell & Bergin (2011a, 2011b) is used to compute the UV and X-ray radiation fields using the UV spectrum from TW Hya and a total X-ray luminosity of $10^{29.5} \text{ erg s}^{-1}$ between 1 and 20 keV as inputs. Gas temperatures are estimated based on (1) the local UV flux and (2) the gas density using fitting functions to the thermochemical models of Bruderer (2013), as described in Cleeves et al. (2015). For cosmic-ray ionization, we used the solar system minimum model from Cleeves et al. (2015). The incident rate at the disk surface is $1.1 \times 10^{-18} \text{ s}^{-1}$ and modulated with vertical depth in the disk. Figure 1 shows the structure of the modeled disk.

2.2. Chemical Model

The physical conditions present in cold, interstellar environments limit the viable chemistry to exothermic reactions with no activation energy barriers. However, certain reactions that are slightly endothermic or have moderate activation energy barriers, so-called high-temperature reactions, may become important in protoplanetary disks where temperatures can reach hundreds to thousands of kelvins near the central star and/or at the disk surface. Infrared observations probe these warmer disk regions; therefore, including high-temperature reactions in our network is crucial. We incorporated high-temperature gas-phase reactions (appropriate for up to 800 K) from Harada et al. (2010) into the gas–grain chemical reaction network of Cleeves et al. (2018), used for the interpretation of submillimeter/millimeter observations of molecular species in protoplanetary disks. We also updated the model’s photodissociation cross-section data based on Heays et al. (2017). More details regarding these modifications to the chemical model are provided in the Appendices A and B.

The initial abundances assumed for the fiducial model are given in Table 1. Major volatile abundances are based on interstellar ice compositions (Boogert et al. 2015). Because the model is dynamically static, the outcomes of mass transport within the disk are approximated by varying these initial abundances as described in Section 3. In models where refractory carbon is included, destruction via oxidation and UV photolysis is added to the reaction network using the method described for carbonaceous grains by Anderson et al. (2017). Two types of refractory carbon reactions are added to the network: (1) oxidation of carbon atoms

Table 1
Initial Abundances

Species	Abundance	Species	Abundance
H ₂	5.000(−01)	HCN	2.000(−08)
He	1.400(−01)	C ₂ H	8.000(−09)
H ₂ O	8.000(−05)	SO	5.000(−09)
CO	9.920(−05)	CS	4.000(−09)
CO ₂	2.240(−05)	H ₃ ⁺	1.000(−08)
CH ₃ OH	4.800(−06)	HCO ⁺	9.000(−09)
CH ₄	3.600(−06)	Si ⁺	1.000(−11)
N ₂	3.510(−05)	Mg ⁺	1.000(−11)
NH ₃	4.800(−06)	Fe ⁺	1.000(−11)

Note. $a(b) = a \times 10^b$ per total H.

on refractory grain surfaces by O producing CO, with a reaction rate from Lee et al. (2010), and (2) UV photolysis of hydrogenated amorphous carbon surfaces releasing CH₄ in addition to minor amounts of C₂H₂, C₂H₄, and C₂H₆ based on the laboratory measurements of Alata et al. (2014, 2015). The carbonaceous grains are assumed to be spherical with a radius of 0.1 μm and composed of pure carbon in the case of oxidation or hydrogenated amorphous carbon in the case of UV photolysis. The amount of carbon initially stored in refractory form is 3.33×10^{-5} relative to total H, equivalent to roughly 40% of the mass of the small dust population. The chemical models are run for a timescale of 3×10^6 yr.

2.3. Observational Predictions

We compute fluxes for CO₂, C₂H₂, HCN, H₂O, OH, and CH₄ using the Python code `slabspec`, the local thermal equilibrium (LTE) emission model of Salyk et al. (2011). The code is available on GitHub⁹ and archived in Zenodo (Salyk 2020). The `slabspec` code receives its molecular line parameters from the HITRAN database (Gordon et al. 2017). The model uses the slab approximation and takes three inputs: column density, gas temperature, and area. A Gaussian line shape where $\sigma = 2 \text{ km s}^{-1}$ is assumed, the same value used by Salyk et al. (2011) for fitting Spitzer and Keck-NIRSPEC data.

The slab model is run for a series of annuli corresponding to ~ 70 radial grid points in our disk model from 0.2 to 10 au. For each radial slice, the vertical column of a given molecular species is integrated from the disk surface down to a total H₂ gas column density of $1.8 \times 10^{23} \text{ cm}^{-2}$. This threshold is selected as the location where the dust becomes optically thick at infrared wavelengths for a gas-to-dust ratio of 1000 in the disk surface layers given the adopted opacities for our dust mixture. We assume a face-on disk orientation, excluding the effects of disk inclination. An average gas temperature weighted by the surface gas density profile for each molecular species in the vertical (z) direction is used as the input temperature for each annulus.

The flux densities for all of the individually modeled annuli are summed to produce a final spectrum. Single-value reported fluxes are integrated over the wavelength ranges used by Salyk et al. (2011) for Spitzer observations of disks (Table 2). The CH₄ flux density is integrated over a more generous range, from 5.0 to 11.0 μm . We ignore the absorption of midplane continuum emission by surface molecules, which could cause

Table 2
Selected IR Spectral Regions

	Wavelength [μm]
CO ₂	14.847–15.014
C ₂ H ₂	13.553–13.764
HCN	13.837–14.075
H ₂ O	17.190–17.260
OH	23.009–23.308
	27.308–27.764
CH ₄	5.000–11.000

the observed fluxes of optically thick lines to be fainter than those reported here.

3. Results

3.1. Molecular Column Densities and Temperatures

Figure 2 shows the surface column densities and density weighted average gas temperatures versus disk radius for several molecules that are of interest as potential targets for JWST Mid-Infrared Imager (MIRI) Medium Resolution Spectroscopy (MRS; Wells et al. 2015) observations. Figure 2 compares the fiducial disk model described in Section 2 to a model where the gas temperature is set equal to that of the dust and a “heated” disk model where the gas temperature is increased by a factor of 2 throughout the disk prior to the chemical calculations. The additional models are included to estimate the effect of the gas temperature, including a much warmer gas temperature, on the observable emission. The higher temperatures are more in line with those derived from infrared observations of several molecules by Carr & Najita (2011) and Salyk et al. (2011).

When considering the gas column integrated vertically into the disk to a total H₂ column density of $1.8 \times 10^{23} \text{ cm}^{-2}$ (the “surface column”), the average gas temperature at which most of these molecular species reside decreases with radius from about 400 K at 0.2 au to 100 K at 5 au for the fiducial model or 800–900 and 200–300 K, respectively, for the heated disk (Figure 2, top row). At larger radii, the average gas temperatures for HCN and H₂O begin to increase. Relative to the other molecular species shown here, OH abundances are concentrated in higher-temperature regions closer to the disk surface and most affected when gas temperatures are not assumed to be enhanced relative to the dust.

Peak surface column densities range from around 10^{15} to 10^{19} cm^{-2} and vary among different molecular species. In most cases, the surface column density is higher closer to the central star and drops off at larger radii. For HCN, C₂H₂, H₂O, CO₂, and CH₄, this behavior is common among multiple models of inner disk chemistry (e.g., Najita et al. 2011; Walsh et al. 2015; Agúndez et al. 2018). In the fiducial model, the surface column densities of C₂H₂ and CH₄ do not peak significantly at smaller radii and therefore differ from the radial behavior that is typically seen.

The increased gas temperatures in the heated disk model result in higher column densities for H₂O and OH, mostly at radii beyond 1 au, as H₂O freeze-out is prevented. The C₂H₂ and CH₄ column densities also increase, but interior to 1 au, and the HCN column densities are higher at all radii within 10 au for the heated disk. Agúndez et al. (2008) described the chemistry behind the enhanced production of small organic species at high temperatures. Bimolecular reactions of small

⁹ Supplementary materials: <http://github.com/csalyk/slabspec>.

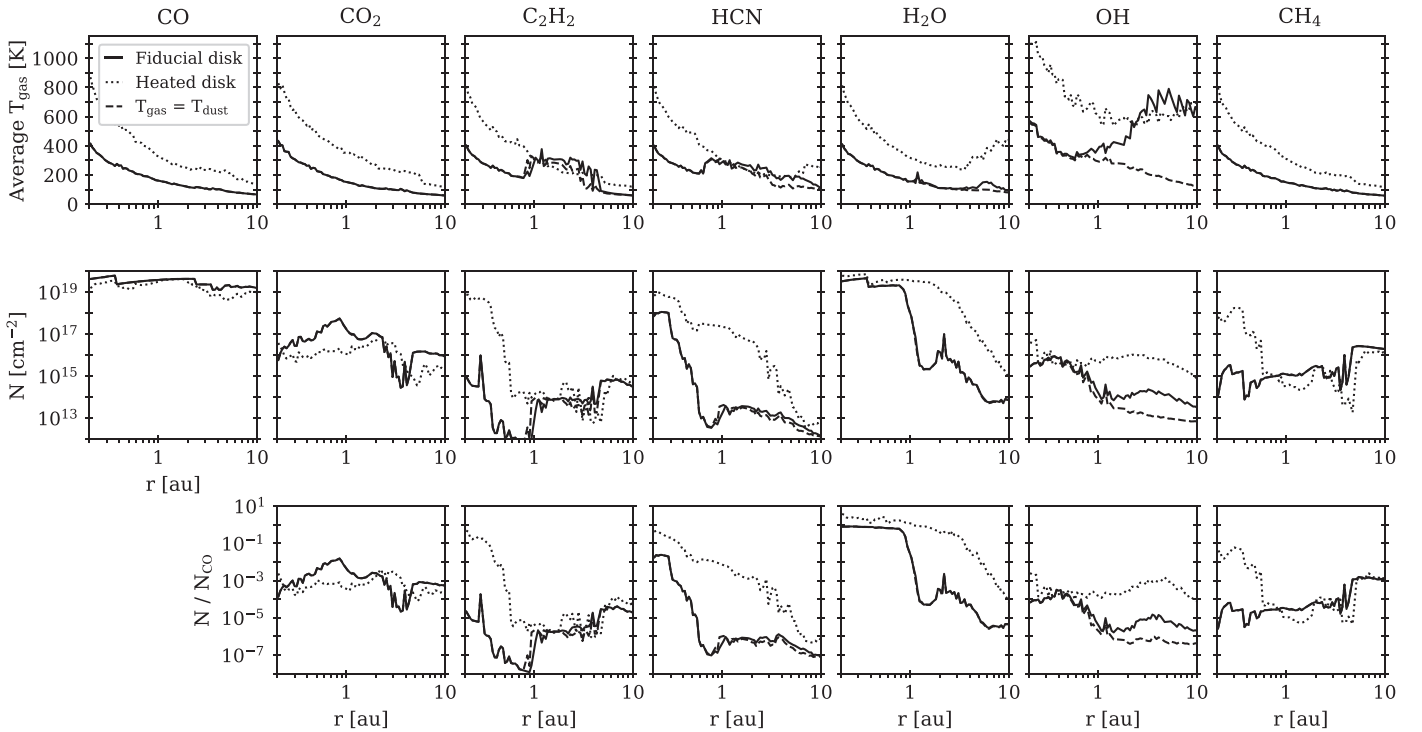


Figure 2. Surface gas density weighted average gas temperature (top row), surface column density (middle row), and surface column density relative to that of CO (bottom row) vs. distance from the central star for observable molecules at 10^6 yr in the fiducial model (indicated with the solid line), a model where disk gas temperatures were increased by a factor of 2 (dotted line), and a model where the gas and dust are thermally coupled (dashed line).

carbon-bearing species (e.g., C^+ , C , CN , and C_2H) with H_2 , which lead to the formation of CH_4 , HCN , and C_2H_2 , have high activation energy barriers. High gas temperatures, above 400–700 K, are required to activate these reactions.

Salyk et al. (2011) derived excitation temperatures >450 – 500 K and up to 1200 – 1600 K from infrared observations of CO , CO_2 , C_2H_2 , HCN , H_2O , and OH in 48 T Tauri disks. Typical observed CO and H_2O column densities were 10^{18} – 10^{19} cm^{-2} , while those of CO_2 , C_2H_2 , HCN , and OH were in the range of 10^{14} – 10^{16} cm^{-2} with a ratio of about 10^{-3} relative to H_2O and CO . Using a slightly different fitting approach, Carr & Najita (2011) found line-of-sight column densities in roughly this same range for H_2O , HCN , and C_2H_2 with derived temperatures of 500 – 800 K based on Spitzer observations of 11 T Tauri disks. Their best-fit temperatures for CO_2 were lower, 100 – 600 K with an average of 350 K, suggesting that CO_2 emission originates in a cooler region radially or vertically in the disk. We do not expect to match the best-fit column densities and temperature values from these works exactly because of the differences in our modeling approaches. Salyk et al. (2011) and Carr & Najita (2011) identified a single column density and temperature over a specified area in the inner disk, where Salyk et al. (2011) used the estimated emitting area of H_2O and Carr & Najita (2011) fit this area separately for different molecules. In comparison, this work models a series of annuli with individual column density and temperature values for disk radii from 0.2 to 10 au. Nevertheless, it is worth noting that our results generally agree with those derived from observations in that the gas is rich in CO and H_2O with somewhat lower column densities of CO_2 , C_2H_2 , HCN , and OH .

Gibb & Horne (2013) observed CH_4 in absorption for the disk around GV Tau N at near-IR wavelengths with a column density of $(2.8 \pm 0.2) \times 10^{17}$ cm^{-2} . The near-IR column density was $2\times$ higher than that of HCN in the same source, with derived rotational temperatures of 750 K for CH_4 and

550 K for HCN . The difference in rotational temperatures suggests that CH_4 abundances peak closer to the central star. As shown in Figure 2, the level of CH_4 in our fiducial model is $\sim 10^{15}$ cm^{-2} . Higher disk gas temperatures are needed to reach the observed value. Although the peak HCN column density is higher than that of CH_4 , the heated disk model does indicate that CH_4 is concentrated at smaller radii, whereas large column densities of HCN are present out to several astronomical units from the star, in agreement with the general behavior noted for GV Tau N.

3.2. Predicted Spectra

The modeled spectra for CH_4 , C_2H_2 , HCN , CO_2 , H_2O , and OH from 4.88 to 30.00 μm , a spectral resolving power $R = 3000$, and the fiducial disk model are provided in Figure 3. For the fiducial model, the HCN , H_2O , and CH_4 emission originates within 1 au from the central star. Some of the CO_2 and C_2H_2 emission comes from larger radii, out to 3 – 5 au. In contrast, a substantial portion of the OH emission comes from radii beyond a few astronomical units from the central star (Figure 4). For comparison, Carr & Najita (2011) derived emitting areas with a radius of about 1 au for H_2O , 0.2 – 0.6 au for HCN , and >0.5 – 2.0 au for CO_2 .

Figure 5 shows the modeled fluxes for C_2H_2 , HCN , CO_2 , H_2O , OH , and CH_4 integrated over the spectral ranges given in Table 2. The outcomes from the fiducial and heated disk models are compared. Increasing fiducial disk gas temperatures by a factor of 2 in the heated disk model causes fluxes to increase by at least an order of magnitude for all six of the molecular species. The CH_4 flux experiences the most extreme difference due to the enhanced temperature. Relative to the molecules that have been detected by Spitzer, the predicted flux for CH_4 is similar for the heated disk model but significantly lower for the fiducial disk.

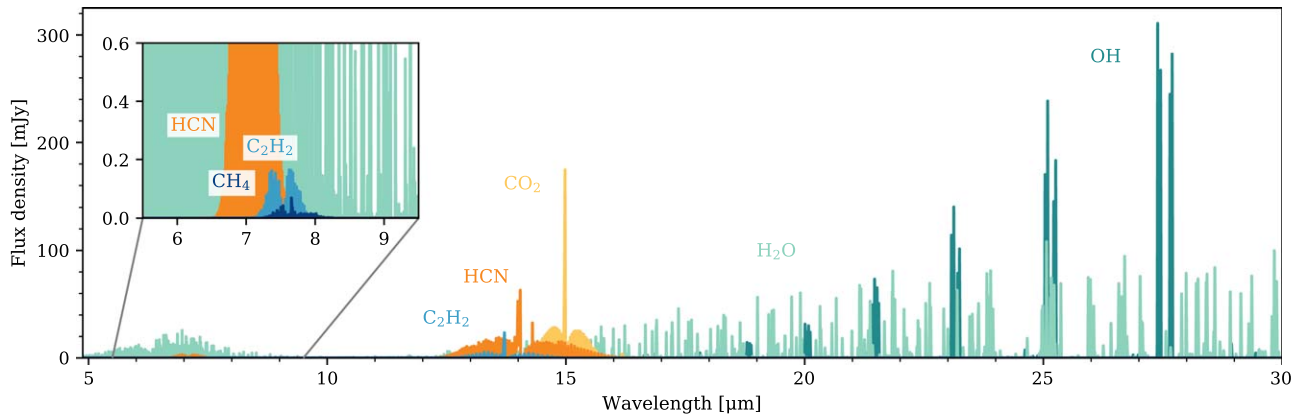


Figure 3. Modeled spectra for CH_4 , C_2H_2 , HCN , CO_2 , H_2O , and OH of the fiducial disk model at 10^6 yr and a distance of 140 pc. Spectra are convolved to a spectral resolving power of $R = 3000$, similar to the resolving power of JWST MIRI MRS. The CH_4 emission is shown in the inset.

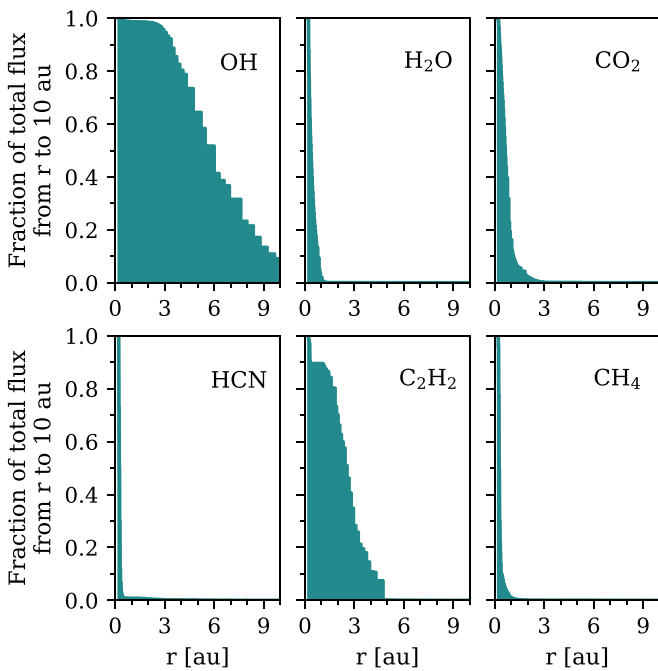


Figure 4. Radial origin of disk emission for molecular species from the fiducial disk model at 10^6 yr. The fluxes modeled for individual annuli are summed over all wavelengths from 4.88 to $30 \mu\text{m}$ and for radii between r and 10 au, then plotted relative to the total flux for all annuli (0.2–10 au).

In comparison to the sample of T Tauri disk fluxes observed by Salyk et al. (2011), the fiducial model fluxes appear within the range of detected values but are relatively high compared to many of the upper limits (Figure 5). This is also true in comparison to the fluxes found by Carr & Najita (2011), although the wavelength ranges used to calculate the integrated fluxes differ slightly. Meanwhile, the heated disk fluxes exceed the observed ranges. For HCN , CO_2 , and H_2O , which have lines that become optically thick at select disk radii in the fiducial model (and all molecules in the heated disk model), absorption of continuum photons at wavelengths where the lines are optically thick may cause the observed fluxes to be smaller than shown here after a standard continuum subtraction is performed. Additionally, line fluxes are affected by the assumed inner gas radius of the disk. Increasing this radius from 0.2 to 1.0 au significantly lowers the fluxes of some molecules, whereas the fluxes of C_2H_2 and OH , both of which

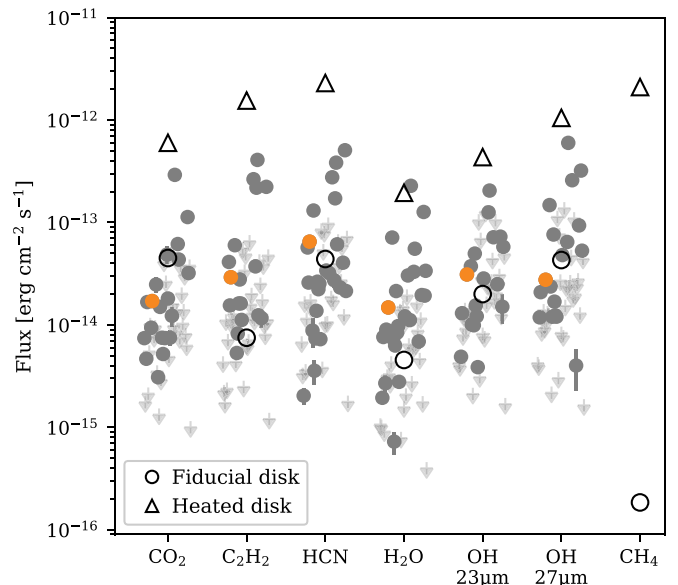


Figure 5. Modeled fluxes for the fiducial model at 10^6 yr and 140 pc integrated over the wavelength ranges in Table 2 (indicated with open circles). The fiducial model fluxes are compared to those from a model where the gas temperatures were increased by a factor of 2 (triangles). Plotted in gray are the observed fluxes from a survey of T Tauri disks by Salyk et al. (2011) for the same molecules and wavelength ranges scaled to a source distance of 140 pc. Downward arrows represent upper limits. Fluxes for AA Tau are shown in orange to indicate an example of the variation within a single source.

have substantial contributions of flux from larger radii (Figure 4), remain largely unaffected (Figure 6).

3.3. Varying Disk Compositions

We now test the dependence of the predicted fluxes on the initial chemical composition of the disk. First, we changed the elemental C/O ratio in the model by altering the initial H_2O abundance. Relative to the disk composition provided in Table 1 with an elemental C/O ratio for volatile materials of 0.57, the initial H_2O abundance was increased by a factor of 10, resulting in a C/O ratio of 0.14, and decreased by a factor of 10 for a C/O ratio of 0.83. With the exception of HCN , the predicted fluxes are sensitive to these changes in the C/O ratio with C_2H_2 displaying the widest range of fluxes (Figure 7). The difference in sensitivity between C_2H_2 and HCN reflects a

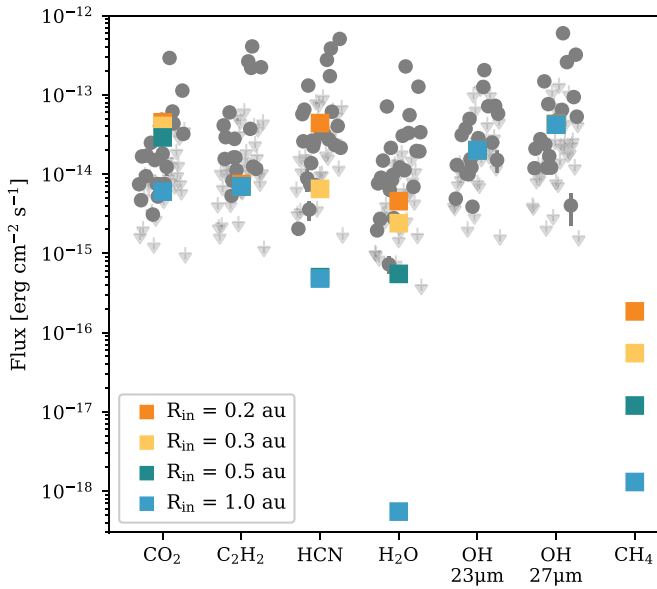


Figure 6. Comparison of fluxes for different inner gas radii in the fiducial model at 10^6 yr and 140 pc integrated over the wavelength ranges in Table 2. Colors indicate different values for the radius of the inner disk gas edge from 0.2–1.0 au. Fluxes were computed by summing the modeled flux per radial bin from the inner edge out to 10 au. Plotted in gray are the observed fluxes from a survey of T Tauri disks by Salyk et al. (2011) for the same molecules and wavelength ranges scaled to a source distance of 140 pc. Downward arrows represent upper limits.

difference in modeled optical thickness for the wavelength regions investigated (given in Table 2).

Next, we changed the elemental C/O ratio by including the destruction of a source of refractory carbon with an initial abundance of 3.33×10^{-5} C atoms relative to total H. This results in a change in the C/O ratio from 0.57 in the fiducial model to 0.71 in the model with carbon grain destruction. Refractory carbon is removed from grain surfaces either by reacting with an oxygen atom at temperatures above a few hundred kelvins producing CO or by a UV photon releasing CH₄ (assuming a starting material of hydrogenated amorphous carbon; Alata et al. 2015). The surface regions interior to 10 au studied here represent an area of the disk where $0.1 \mu\text{m}$ carbon grains are largely destroyed within the disk lifetime. Therefore, by 10^6 yr, the elemental C/O ratio of volatile materials is equal to the total (refractory + volatile) elemental C/O ratio for the model.

As Figure 7 shows, the inclusion of carbon grains in the model generally causes the fluxes of C₂H₂, HCN, and CH₄ to increase and the fluxes of oxygen-bearing species to decrease. This pattern matches that found when increasing the C/O ratio by decreasing the initial H₂O abundance. The effect of including carbon grains on the predicted fluxes increases for lower initial H₂O abundances, making it easier to distinguish the models with and without carbon grains at high C/O ratios.

Changing the disk gas temperatures by a factor of 2 produces larger flux values than altering the C/O ratio within the range of 0.14–1.04 for all molecular species. This is the result of both high-temperature chemical changes as seen in the heated disk surface column densities in Figure 2 and higher excitation temperatures. The range in predicted fluxes for the molecules shown here is about 1 order of magnitude for the heated disk, lower than that for the other modeled scenarios, where differences among the fluxes for different molecular species

are more pronounced. Assuming that the gas temperatures are equal to the dust temperatures decreases the modeled fluxes for C₂H₂ and OH, while other molecular fluxes are not affected.

Finally, we modeled four different initial disk compositions with the same elemental C/O ratio of 0.71. Compared to the fiducial disk composition (Table 1), an excess of 3.33×10^{-5} C atoms relative to total H was added in the form of (1) refractory carbon grains as described above, (2) CH₄, (3) CH₃OH, and (4) CO₂. In the cases of CH₃OH and CO₂, the initial H₂O abundance was reduced relative to the fiducial model in order to achieve a C/O ratio of 0.71. The predicted fluxes are largely the same among these four models (Figure 7), indicating a lack of sensitivity to the relative abundances of initial carbon carriers.

3.4. Surface versus Midplane Composition

Here we compare the composition of the disk surface to that of the midplane over time. Figure 8 shows this comparison at 1 au from the central star for the models exploring different relative amounts of initial carbon carriers (Section 3.3). At the final simulation time step of 3×10^6 yr, the chemical composition of the disk surface gas converges for all four models, regardless of the initial distribution of elemental abundances among molecular species. When excess carbon is introduced in the form of CH₄, CH₃OH, or CO₂ in photon-dominated regions near the disk surface, these molecules are quickly destroyed by photodissociation or reactions with ionized species. Here ionized species are largely generated as a result of the ionization of H₂ and He via X-rays. Carbon is eventually transferred to CO. Meanwhile, oxygen is transferred from H₂O, CO₂, and CH₃OH to CO, O, and O₂. Note that the relative importance of H₂O gas and ice, CO, O, and O₂ as oxygen carriers in this surface layer depends on the disk radius.

In models that include destruction of carbon grains, UV photolysis at the disk surface releases CH₄, which is then converted to CO. In atomic O-rich regions where the temperature is above a few hundred kelvins, oxidation of refractory carbon can also produce CO directly. For the location shown in Figure 8, carbon release occurs more slowly from the refractory form than from CH₄, CH₃OH, or CO₂, causing the carbon grain model to take somewhat longer to equilibrate.

In the case of the disk surface layers at 1 au, regardless of the initial carbon carriers, more than 99% of the available carbon ultimately ends up being stored in CO. For most of the molecular species shown in Figure 8, steady-state abundances are reached around $\sim 10^4$ yr. The specific conversion timescale will depend on the location within the disk and the local UV radiation environment.

Midplane abundances of the major carbon carriers (CO, CO₂, CH₄, and CH₃OH) experience relatively less and in some cases no change over a timescale of 10^6 yr at 1 au (Figure 8, solid lines). Unlike in the surface layers, final abundances of the major carbon carriers in the midplane tend to reflect the initial composition provided to the model. The reason for this slower chemistry is that in denser regions, shielded from UV and X-ray photons, a combination of cosmic-ray ionization and ion chemistry together control the destruction of CH₄, CH₃OH, and CO₂. Therefore, midplane chemistry is largely dependent on the degree of ionization in these dense disk regions. The cosmic-ray ionization rate is not well constrained for most protoplanetary disks. The interstellar value for ionization of H₂

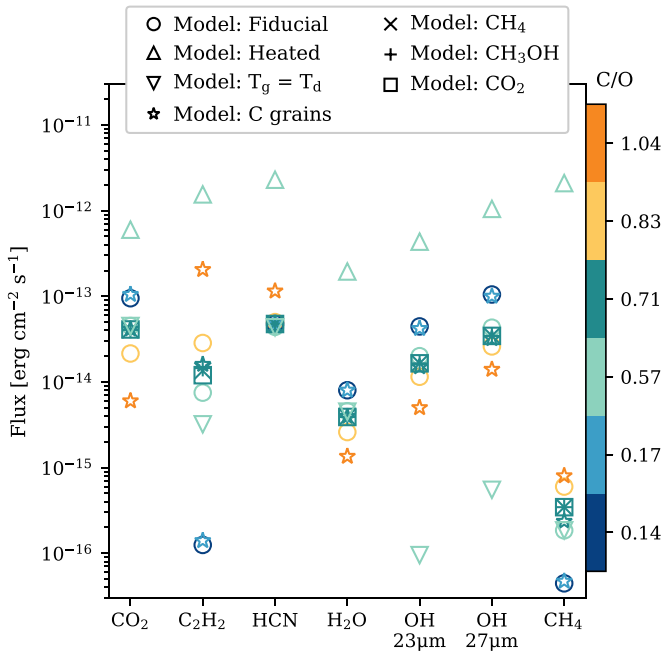


Figure 7. Comparison of fluxes for several models at 10^6 yr and 140 pc integrated over the wavelength ranges in Table 2. Colors indicate C/O ratios, and symbols indicate the following initial conditions: models based on the fiducial setup where the C/O ratio is determined by varying the H_2O abundance (indicated with open circles; note that the composition in Table 1 corresponds to a C/O ratio of 0.57), models including the destruction of refractory carbon grains (stars), three additional models with a C/O ratio of 0.71 but different relative amounts of major carbon carriers (crosses, plus signs, and squares; see Section 3.3 of the text for more details), and models where the disk gas temperature was increased by a factor of 2 (upward triangles) or set equal to the dust temperature (downward triangles) and the initial composition is given in Table 1.

is around $3 \times 10^{-17} \text{ s}^{-1}$ but may be decreased stellar winds or magnetic fields of young accreting T Tauri stars. The H_2 cosmic-ray ionization rate has been estimated to be $\lesssim 10^{-19} \text{ s}^{-1}$ based on observations of ionized species for the disk of TW Hya (Cleeves et al. 2015).

As a test case, we started our model with all of the initial volatile carbon in the form of CH_3OH ice. At 10^6 yr and 1 au in the disk midplane, around 20% of the carbon was transferred to other chemical species when using an interstellar cosmic-ray ionization rate, whereas none of the carbon was removed from the original carrier for an H_2 cosmic-ray ionization rate of 10^{-19} s^{-1} . These findings of a halted midplane chemistry at low cosmic-ray ionization rates are consistent with those of Cleeves et al. (2014), Eistrup et al. (2018), and Price et al. (2020).

Finally, we explore what would happen if, due to vigorous mixing, the chemical composition of the surface were introduced into the midplane. Essentially, we want to see if the surface composition would return to a state that looks like that of a static midplane model. Figure 9 compares midplane chemical abundances for the static model initiated with interstellar ices (Table 1) to a model where the initial composition reflects the disk surface composition at a height of 0.15 au above the disk midplane for a radius of 1 au (Table 3).

Note that there are multiple major carbon carriers in the midplane for the fiducial disk. At 1 au, most of the total carbon is stored in CO, but carbon is also found in CO_2 at the 10% level and both CH_3OH and CH_4 at single-digit percentages. In contrast, CO is by far the dominant carbon carrier for the disk

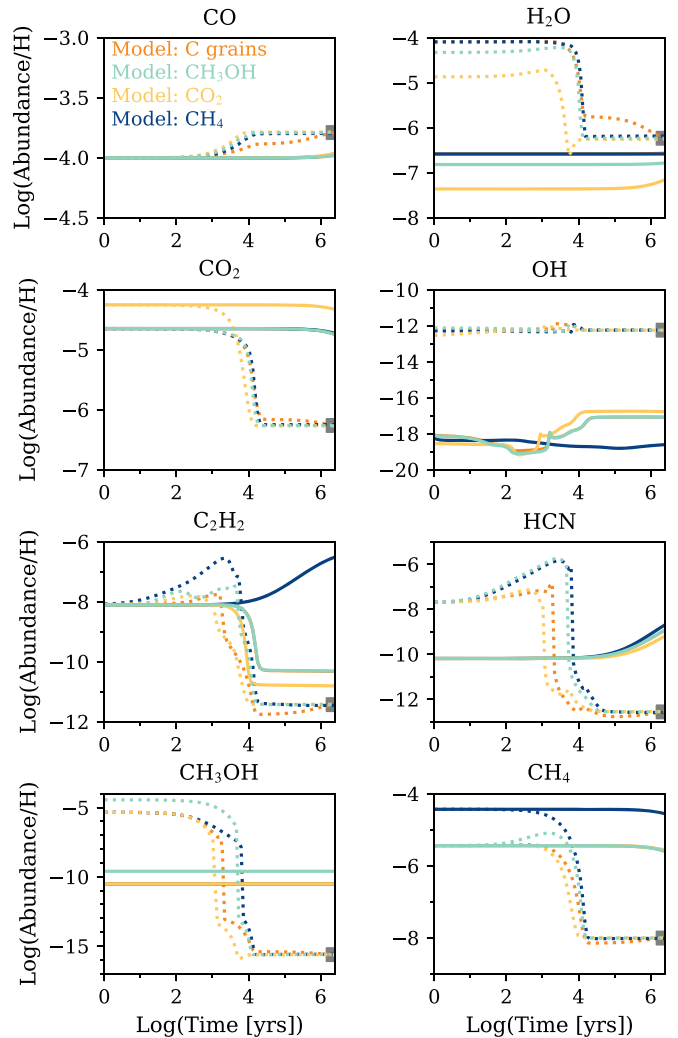


Figure 8. Fractional abundance of several chemical species relative to total H over time plotted for four modeled scenarios with the same total elemental C/O ratio but different initial compositions (see Section 3.3). Abundances are compared for two disk locations at 1 au from the central star: the midplane (solid lines) and 0.15 au above the midplane (dotted lines). Gray squares highlight the steady-state surface abundance to which all of the models converge.

model with an initial surface-like composition (Figure 9). We find that even over 3×10^6 yr, the midplane abundances of CO_2 , CH_3OH , and CH_4 in the model with an initial surface-like composition do not approach the levels seen in the fiducial disk initialized with interstellar ices. Therefore, if vigorous mixing is present, then it is possible that the entire column of material in the inner disk will tend toward the CO-dominated composition of the surface (see discussion in Section 4.3).

4. Discussion

4.1. Predictions for JWST MIRI

In this section, we use our modeled fluxes for CO_2 , C_2H_2 , HCN, H_2O , OH, and CH_4 to consider what will be possible with JWST MIRI. While MIRI is not the only JWST instrument that will be able to do molecular gas science in protoplanetary disks, the broad wavelength coverage and high sensitivity make it an excellent tool to survey the diversity of disk gas compositions. With the exception of CH_4 , all of the

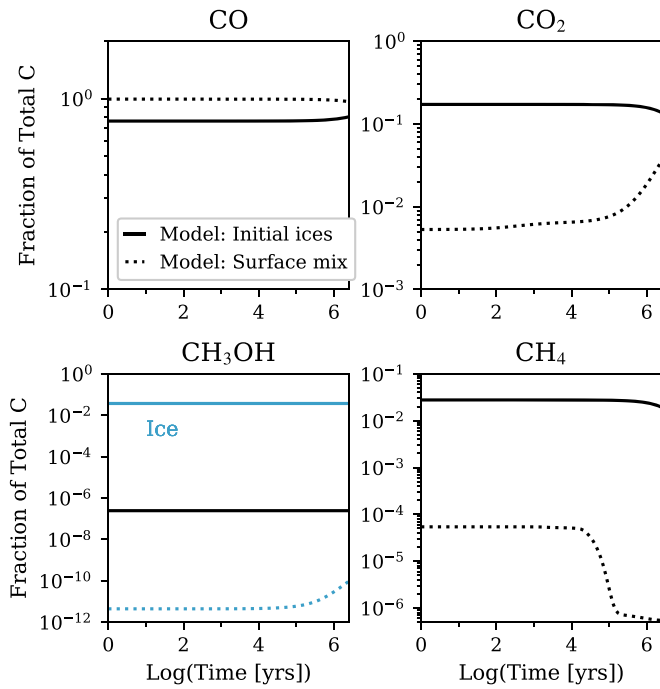


Figure 9. Fraction of the total carbon over time in CO, CO₂, CH₃OH, and CH₄ in the midplane at 1 au. Models with different initial compositions are compared, including the fiducial disk composition (Table 1, solid line) and a disk surface-like composition (Table 3, dotted line). Ice abundances are shown in blue.

Table 3
Disk Surface Abundances at 1 au^a

Species	Abundance	Species	Abundance
H ₂	5.000(-01)	HCN	2.000(-08)
He	1.400(-01)	C ₂ H	8.000(-09)
H ₂ O	1.753(-06)	SO	5.000(-09)
CO	1.293(-04)	CS	4.000(-09)
CO ₂	6.854(-07)	H ₃ ⁺	1.000(-08)
CH ₃ OH	4.000(-16)	HCO ⁺	9.000(-09)
CH ₄	7.026(-09)	Si ⁺	1.000(-11)
N ₂	3.738(-05)	Mg ⁺	1.000(-11)
NH ₃	1.586(-09)	Fe ⁺	1.000(-11)
O ₂	4.015(-05)	O	1.606(-05)
N	2.601(-07)		

Note. $a(b)=a \times 10^b$ per total H.

^a For the fiducial model at $z = 0.15$ au.

above-mentioned molecules have been observed in emission from T Tauri disks with Spitzer. Therefore, JWST should be able to readily detect them and provide a statistical picture of disk chemistry.

The potential to observe CH₄ is more unique to JWST; however, we find it will be challenging. Particularly for gas temperatures similar to those in the fiducial disk model, we expect that CH₄ will be more difficult to detect than the other molecular species because of low absolute fluxes and low fluxes relative to other species with overlapping emission features. Figure 10 compares the modeled CH₄ emission to multiple line-to-continuum thresholds. The CH₄ feature overlaps with emission from C₂H₂, HCN, and H₂O and is generally much weaker than that of the interfering molecular species.

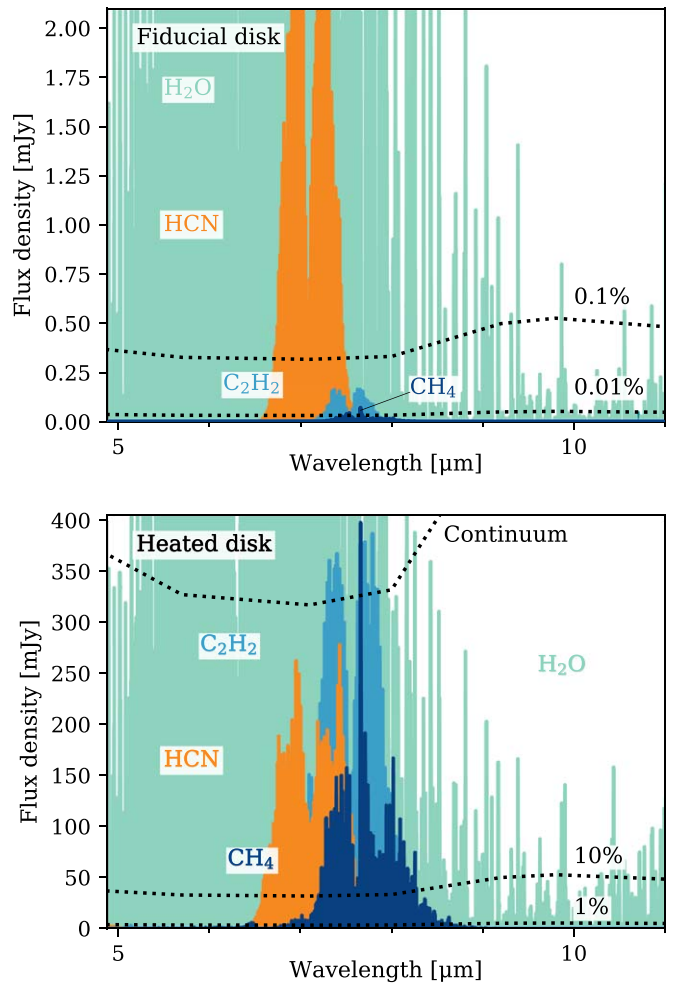


Figure 10. Zoom-in of spectra around the CH₄ feature for the fiducial model (top) and the model with artificially enhanced gas temperatures (bottom). Dotted lines indicate the level of the continuum flux density, assumed to equal the median spectral energy distribution for low-mass stars in Taurus (Furlan et al. 2006) and fractions thereof. A signal-to-noise ratio $\gg 1000$ would be required on the continuum to detect the CH₄ peak for the fiducial model, whereas the level of CH₄ emission for the heated disk is easily detectable.

Only in the case of the artificially heated disk does CH₄ emission appear in the detectable range. Increasing the C/O ratio of the disk also helps by increasing the peak height of the CH₄ feature (see Appendix C).

Detected flux ratios among all molecular lines observed by Carr & Najita (2011) and Salyk et al. (2011) with Spitzer generally fall in the range of 0.1–10. Overall, this is more consistent with models that have C/O ratios of 0.57–0.83, a full inner gas disk, and gas temperatures that are warmer than those of the dust (Figure 11). In comparison, the C/O ratios furthest from the solar value result in much larger ranges in line flux ratios, spanning from 0.001 to 1000 in the case of C/O = 0.14, for example. Given the current observational data, it appears that the modeled disk with an inner gas radius of 0.5 au is inconsistent with the observed limits on the C₂H₂/HCN and OH/H₂O flux ratios. In addition, the low OH fluxes in the model where the gas and dust are thermally coupled cause the flux ratios relative to OH to fall outside the observed range. However, this scenario cannot be ruled out given the unconstrained limits. The improved sensitivity of

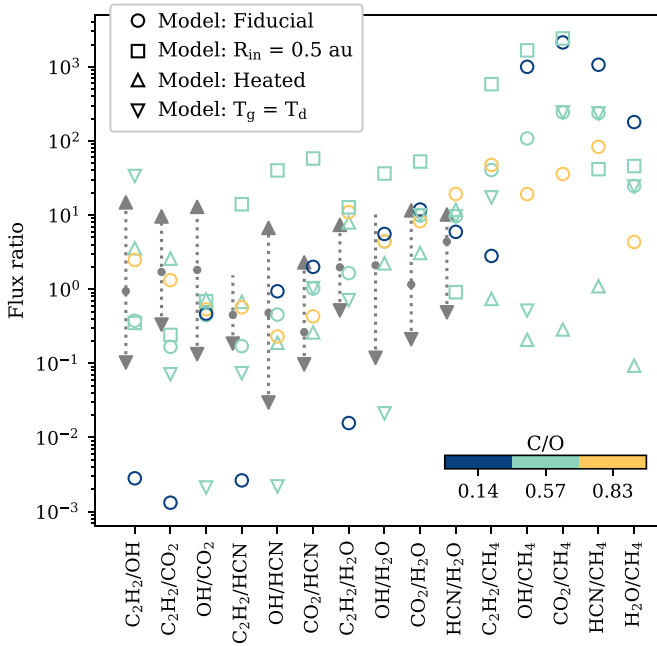


Figure 11. Comparison of relative fluxes among C_2H_2 , OH ($23\ \mu\text{m}$), CO_2 , HCN, H_2O , and CH_4 for Spitzer observations (Salyk et al. 2011) vs. our modeled scenarios. Observed fluxes were included for disks where two or more spectral lines were detected. The range of observed values or limits is shown, with arrows indicating where upper or lower limits were included. Gray dots represent the values for AA Tau as an example of the flux ratios within a single source. Model results are provided with colors indicating different C/O ratios and symbols indicating the following initial conditions: the fiducial physical disk model (circles), models where the disk gas temperature was increased by a factor of 2 (upward triangles) or set equal to the dust temperature (downward triangles), and assuming an inner gas radius of 0.5 au instead of 0.2 au (squares).

JWST will provide access to a larger range of flux ratios and further constraints.

Many line flux ratios show sensitivity to the C/O ratio, but these trends could often be conflated with changes in gas temperature or the inner disk gas radius. The HCN/ H_2O flux ratio is the most consistent in tracking the C/O ratio, showing a lack of sensitivity to the variations in gas temperature tested here (Figure 11). HCN/ H_2O has previously been identified as a promising tracer of the C/O ratio in the inner regions of disks (Carr & Najita 2011). Although this flux ratio is also sensitive to the inner disk gas radius in our models, the disparity between the C_2H_2 , OH, and CO_2 fluxes and those of HCN, H_2O , and CH_4 separates changes to this parameter from those to the C/O ratio. Whereas the C/O ratio reflects the composition of the gas, indicators of the inner gas edge will depend on differences in the emitting regions of the molecules. The high CH_4 fluxes in the heated disk cause flux ratios of other molecules relative to CH_4 to be 0.1–1.0, generally lower than those in cooler disk models. Therefore, CH_4 may be an indicator of different temperature regimes.

4.2. Uncertainties in the Predicted Molecular Column Densities and Fluxes

The actual column of material that is sampled via observations at infrared wavelengths will depend on the opacity of the dust and contributing gas species in the disk. The assumed H_2 surface column density of $10^{23}\ \text{cm}^{-2}$ could

vary by up to a factor of ~ 10 for bounding scenarios of pure silicate or graphite grains or, alternatively, when assuming that the total disk dust mass is present in small ($\lesssim 1\ \mu\text{m}$) grains. Given the steep gas density gradient in the vertical direction and chemical transitions that depend on the vertical profiles of the disk temperature and radiation field, predicted molecular column densities are very sensitive to the assumed depth of the surface column probed by infrared observations. Probing deeper into the disk would mean higher molecular column densities and compositions that are influenced by that of the shielded midplane. Alternatively, if observations probe a more limited region closer to the disk surface, then molecular column densities would be lower and the timescales for converting refractory and volatile carbon carriers into CO would be $< 100\text{--}1000\ \text{yr}$ at 1 au.

In addition, the exclusion of non-LTE effects may be a limitation of this work. LTE models have been used to interpret Spitzer observations of line emission from numerous disks (e.g., Salyk et al. 2011; Carr & Najita 2011). Modeling of mid-infrared H_2O emission by Meijerink et al. (2009) suggests that including the decoupling of gas and dust counteracts the effects of a non-LTE treatment. A simple approach ignoring both gas decoupling and non-LTE effects may therefore be sufficient for H_2O . Meanwhile, detailed studies focused on HCN and CO_2 have predicted differences in IR band fluxes by up to a factor of 3 when using LTE versus non-LTE models (Bruderer et al. 2015; Bosman et al. 2017). Our predictions are unlikely to be as strongly affected because our modeled molecular abundances drop off sharply in the tenuous surface layers of the disk where non-LTE effects are most important (see discussion by Woitke et al. 2018).

4.3. Tracking C and O Carriers in Disks

The insensitivity of the surface composition to initial abundances allows for determination of the elemental C/O ratio in the inner disk based on molecular tracers. This ratio will be useful for indirectly tracking changes in the disk composition and for observational comparisons between disks and planetary atmospheres. Planet compositions are traditionally considered to be the product of disk midplane materials, but some contribution may also be derived from larger scale heights via vertical accretion (e.g., Teague et al. 2019; Cridland et al. 2020). The relative importance of the surface chemistry will depend on the flow rate of material from the surface. Given that surface chemistry erases the assumed initial abundances in our models within the disk lifetime (e.g., Figure 8), it is possible that the relative abundances of molecular species derived from infrared observations may not be representative of the composition of planet-forming regions in the disk midplane.

The degree to which separate molecular compositions can be maintained in the surface versus midplane will depend on the efficiency of vertical mixing. The diffusion timescale for a single scale height at 1 au is about 15 yr based on the formula for the diffusion coefficient of gas from Dullemond & Dominik (2004) and turbulence characterized by a standard α value of 0.01. However, uncertainty in the diffusion coefficient by orders of magnitude could largely vary this timescale estimate. The competing chemical timescale, the timescale needed to reach a steady-state surface composition, decreases sharply with height above the midplane and depends on the strength of

the local UV radiation field. If the bulk of the midplane materials reach a height where the surface chemistry occurs much more rapidly than the mixing timescale, the entire vertical column may adopt a more surface-like, CO-dominated composition (e.g., Figure 9).

Whereas infrared observations find that gas in the inner regions of T Tauri disks is CO-rich (Salyk et al. 2011), detections of the H₂ isotopologue hydrogen deuteride (HD) in three disks by the Herschel Space Observatory combined with submillimeter observations of CO isotopologues from the Submillimeter Array (SMA) and the Atacama Large Millimeter/submillimeter Array (ALMA) resulted in estimated cold disk CO/H₂ ratios of up to 100× below the interstellar value of $\sim 10^{-4}$ (Bergin et al. 2013; Favre et al. 2013; McClure et al. 2016). The apparent lack of gas-phase CO in the outer disk is not an uncommon finding. Earlier suggestions of CO depletion were made based on weak CO relative to millimeter continuum emission for disks BP Tau (Dutrey et al. 2003), CQ Tau, and MWC 758 (Chapillon et al. 2008). In addition, total gas mass estimates based on observed CO emission are found to be lower than those based on submillimeter/millimeter dust assuming a gas-to-dust mass ratio of 100 for numerous disks in recent ALMA surveys (e.g., Miotello et al. 2017). Studies of multiple disk gas tracers have also found examples of disk compositions that are consistent with a subinterstellar CO abundance (Cleeves et al. 2018; Anderson et al. 2019).

Some loss of gas-phase CO is expected as a result of freeze-out in cooler regions of the disk ($T \lesssim 20$ K) and photodissociation of CO at regions with low UV extinction. But radial distributions of CO obtained from spatially resolved ALMA observations of its isotopologues in the TW Hya disk show significant depletion relative to interstellar values even interior to the CO snow line and near the disk midplane (Schwarz et al. 2016; Zhang et al. 2017). An alternative explanation for the lack of CO is that chemical processes occurring in protoplanetary disk environments result in the sequestration of CO into less volatile carbon species over time (Bergin et al. 2014; Furuya & Aikawa 2014; Reboussin et al. 2015; Yu et al. 2016; Eistrup et al. 2016). Schwarz et al. (2018) found that chemical reprocessing can account for up to an order of magnitude of CO depletion under the right disk conditions, but reaching the levels of depletion suggested by the aforementioned HD measurements requires additional non-chemical processes, such as trapping of CO in cooler regions via vertical mixing or into large, kilometer-sized bodies forming in the disk (Krijt et al. 2018; Zhang et al. 2019). Potential products of the chemical reprocessing of CO ice in protoplanetary disks are CH₃OH, CO₂, and CH₄ ices (Schwarz et al. 2018; Bosman et al. 2018b). Our modeling suggests that such products would be converted to CO in a fraction of the disk lifetime in the inner disk surface layers probed at infrared wavelengths. Therefore, if chemical conversion is responsible for the “missing” CO in the outer disk, and this carbon is retained in other volatile forms, it should become detectable again in infrared observations.

The carbon carriers from the outer disk could be introduced into the inner disk via radial drift. Radial drift occurs when dust grains in the disk grow large enough to decouple from the gas and begin to drift radially inward as a result of the difference in velocity between the dust and the slower-moving, pressure-supported gas. This transport of materials may influence the composition of the inner disk (e.g., Bosman et al. 2018a;

Zhang et al. 2020; Banzatti et al. 2020). Contributions from larger radii via radial drift will depend on the partitioning of materials between the gas and solid phases in the outer disk. An influx of H₂O-rich ices (e.g., Ciesla & Cuzzi 2006) could enhance H₂O abundances (and lower the C/O ratio) in the inner disk. Alternatively, H₂O could be locked up in large solid bodies, reducing the amount of oxygen (and raising the C/O ratio; Najita et al. 2013). Refractory carbon materials or carbon-rich ices could also be delivered from the outer disk. Signatures of inward radial drift may be preserved in the gas if resupply occurs on a timescale of $<10^3$ – 10^4 yr based on the time needed for an initial excess of carbon in grains, CO₂, CH₃OH, or CH₄, to be depleted in the inner few astronomical units, as seen in Figure 8. Even if direct signatures are erased, the C/O ratio could provide indirect evidence for dynamical processes. Combining such evidence from infrared observations with those at longer wavelengths (e.g., ALMA or the future Square Kilometre Array) will be important for determining the distribution of major carbon and oxygen carriers throughout the planet-forming regions of protoplanetary disks.

5. Conclusion

We present models of different chemical compositions in the inner regions of protoplanetary disks and predict how they will affect the fluxes of a set of observable carbon and oxygen tracers at mid-infrared wavelengths. Our results will inform future investigations of protoplanetary disks by observatories such as JWST. Here we summarize our conclusions based on these analyses.

Our models show that, in the absence of mass transport, the composition of the inner disk surface (for radii of up to a few astronomical units) is dominated by UV and X-ray photon-driven chemistry, which largely resets the initial chemical state on a timescale less than the characteristic bulk disk gas lifetime of a few million years. Here CO is the dominant carbon carrier in the inner disk steady-state surface composition regardless of the initial distribution of carbon among major carbon-bearing disk species (i.e., CO, CO₂, CH₃OH, CH₄, and small refractory carbon grains). This conversion of less volatile carbon species to CO could explain the apparent discrepancy between CO-poor gas observed in the outer regions of protoplanetary disks by ALMA relative to the predominately CO-rich gas observed at infrared wavelengths. In contrast, midplane compositions reflect the initial chemical abundances (when disk dynamics are excluded). The degree to which the original carbon carriers are converted to different chemical species in the midplane is largely driven by ion chemistry and therefore tied to the cosmic-ray ionization rate.

Actual inner disk compositions will depend on the scale and efficiency of mass transport processes in the disk. Efficient vertical transport of materials may result in the destruction of materials that would otherwise be preserved over the disk lifetime if left in the midplane. Because a gas of surface-like composition will not return to the average disk midplane composition in less than $\sim 10^6$ yr, this could potentially result in the entire vertical column appearing more surface-like in composition. Rapid resupply of icy and refractory carbon-rich solids via radial drift on timescales of less than 10^3 – 10^4 yr could also alter inner disk (radii ~ 1 au) surface compositions.

Infrared observations may not directly probe the relative abundances of specific major carbon and oxygen carriers in the shielded planet-forming regions of protoplanetary disks. However, the predicted fluxes of C_2H_2 , HCN, CO_2 , H_2O , OH, and CH_4 are sensitive to changes in the C/O ratio, inner gas radius, and gas temperature of the disk. In particular, the HCN/ H_2O flux ratio appears to be a good tracer of the disk C/O ratio even in different gas temperature regimes. Furthermore, molecular flux ratios relative to CH_4 may serve as an indicator of the gas temperature. Although we only considered the use of total integrated fluxes here, additional constraints on the location and temperature of disk emission will be available via line shapes in spectrally resolved observations. These results are promising for future comparisons of C/O ratios with the atmospheres of extrasolar gas giant planets and investigating the physical conditions of the inner regions of protoplanetary disks.

The authors thank the anonymous reviewer for providing helpful suggestions. D.E.A. acknowledges support from the Virginia Initiative on Cosmic Origins (VICO) Postdoctoral Fellowship. L.I.C. gratefully acknowledges support from the David and Lucile Packard Foundation, the Virginia Space Grant Consortium, Johnson & Johnson’s WiSTEM2D Award, and NSF AAG grant No. AST-1910106. G.A.B. acknowledges support from the NASA XRP program (NNX16AB48G).

Software: Astropy (Astropy Collaboration et al. 2013; Price-Whelan et al. 2018), Matplotlib (Hunter 2007), Numpy

(van der Walt et al. 2011), Pandas (Reback et al. 2021), parallel (Tange 2018), slabspec (Salyk 2020).

Appendix A Updates to Reaction Network

Additional cosmic-ray, positive ion-neutral, neutral-neutral, electronic dissociative recombination, and photodissociation reactions were added from the OSU high-temperature network of Harada et al. (2010). As a result, 11 new species were added, including carbon chains with 10 C atoms, C_2H_6 , $C_2H_7^+$, and HN_2O^+ . In addition, for select positive ion-neutral and ion-neutral radiative association reactions, the temperature dependence of the reaction rate was altered to provide appropriate rates above 300 K (see Harada et al. 2010). Rates for UV photolysis induced by X-rays were also added for additional species based on efficiency values for cosmic-ray-induced photoreactions from the UMIST database (McElroy et al. 2013).

Of the 653 chemical species modeled, about 80% experienced more than a 30% change in their column densities for at least three consecutive radial grid points from 0.2 to 10 au. This is true when considering either the surface column density (calculated as described in Section 2.3) or the total column density (calculated from the disk surface to the midplane). The percentage of species decreases to 67% for changes by greater than a factor of 10. Chemical species containing multiple carbon atoms were among the most affected. Figure 12 compares the modeled column densities for the main species

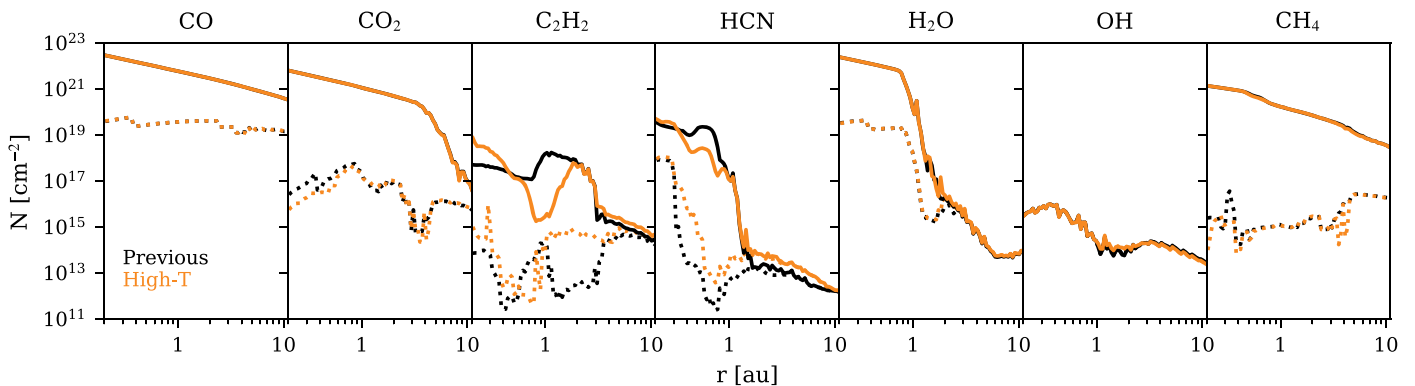


Figure 12. Comparison of the surface column densities (dotted lines) and total column densities (from the surface to the midplane; solid lines) vs. disk radius based on the previous reaction network (shown in black) to those based on the updated network incorporating high-temperature reactions (shown in orange).

investigated in this work. The largest changes are seen for C_2H_2 and HCN.

Appendix B Updates to Photodissociation Cross Sections

Updated photodissociation cross-section data are from Heays et al. (2017). The continuum was interpolated across the range of 912–2000 Å with wavelength intervals of 10 Å. Narrow lines were added to the appropriate wavelength bins. Photodissociation rates were calculated based on the UV field and cross section, as described in Fogel et al. (2011).

We added wavelength-dependent photodissociation cross sections for C_2 , C_2H_3N , C_2H_4 , C_2H_4O , C_2H_5OH , C_3H , C_3H_2 , C_4 , C_4H , C_5H , CH_2 , CH_3 , CH_3OH , CH_5N , CO_2 , CS , H_2^+ , H_2C_3 , H_2CO , H_2O_2 , H_2S , H_3^+ , HC_3 , HC_3N , HCO , HCl , HF , N_2O , NH_2CHO , NO_2 , OCS , OH^+ , PH , SO , SiH , SiH^+ , and SiO . The value for the linear isomer is used except in the cases of C_3H_2 (cyclic) and H_2C_3 (linear) and C_3H (cyclic) and HC_3 (linear), where both isomers are present in the network. We updated the wavelength-dependent photodissociation cross-section data for C_2H_2 , C_3 , CH_4 , CN , H_2O , HCN (the same was used for HNC), NH , NH_2 , NH_3 , NO , O_2 , and SO_2 . The remaining species for which photodissociation rates are calculated based on wavelength-dependent rates from the

literature include C_2H , C_4H_2 , CH , CH^+ , and OH . The treatment of H_2 , CO , and N_2 self-shielding remains the same relative to previous versions of the model (see Fogel et al. 2011; Cleeves et al. 2018).

Updating the photodissociation cross sections for the above listed species generally had a larger effect on the surface column densities than on the total column densities for modeled species. Of the 653 chemical species modeled, about 70% experienced a change by more than 30% in their surface column densities for at least three consecutive radial grid points from 0.2 to 10 au, whereas only about 50% experienced this level of change in their total column densities (calculated from the disk surface to the midplane). For changes over an order of magnitude, these percentages are 30% and 20%, respectively. In many cases, the amount of change was radially dependent. Among the species for which cross-section data were updated in the model, the largest changes to surface column densities were for carbon-bearing species, in particular hydrocarbons, at select radial regions interior to 5 au. For the main species investigated in this work, differences in computed surface column densities due to the updated cross sections were less than a factor of 2–3 and limited to the inner 5 au from the central star. The exception was C_2H_2 , having over an order of magnitude decrease in the surface column density in the region around a few astronomical units (Figure 13).

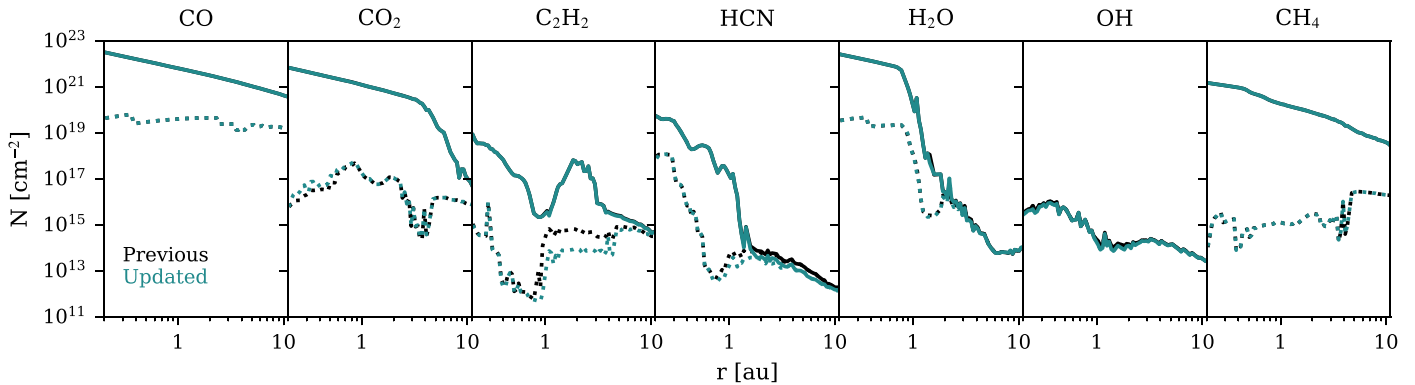


Figure 13. Comparison of the surface column densities (dotted lines) and total column densities (from the surface to the midplane; solid lines) vs. disk radius when using the previous photodissociation cross-section data (shown in black) to those modeled when using the updated data (shown in teal).

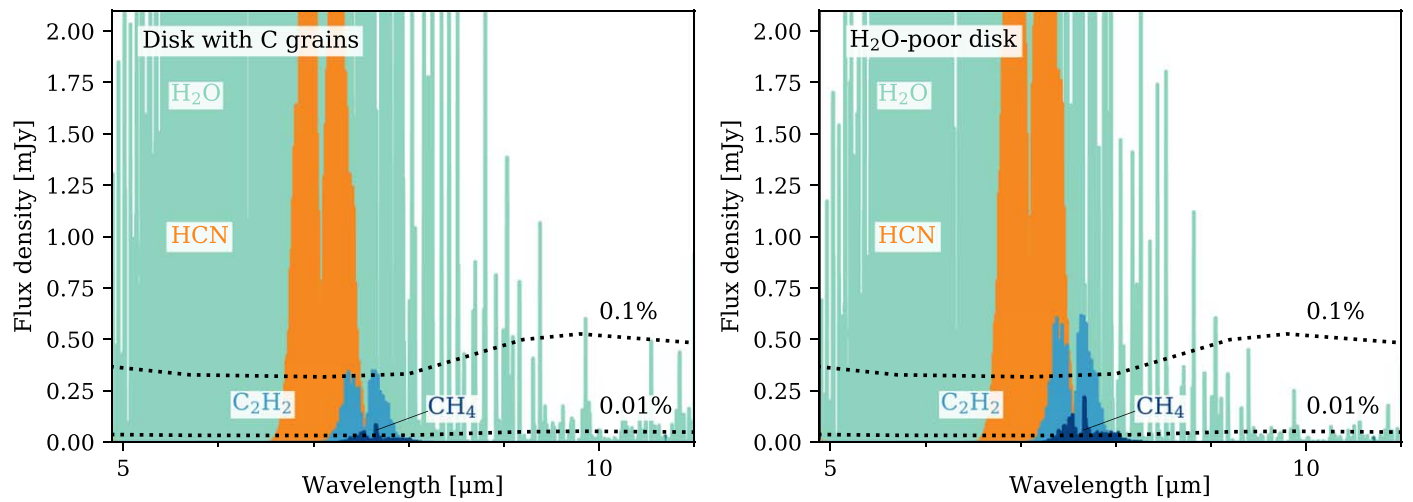


Figure 14. Zoom-in of spectra around the CH₄ feature for the model including destruction of refractory carbon grains (left) and the model with initial H₂O abundances decreased by 10 \times (right). Dotted lines indicate fractions of the continuum flux density, assumed to equal the median spectral energy distribution for low-mass stars in Taurus (Furlan et al. 2006).

Appendix C Observability of Methane

Figure 14 is a continuation of Figure 10 including additional models with different elemental C/O ratios.

ORCID iDs

Dana E. Anderson <https://orcid.org/0000-0002-8310-0554>
 Geoffrey A. Blake <https://orcid.org/0000-0003-0787-1610>
 L. Ilseidore Cleeves <https://orcid.org/0000-0003-2076-8001>
 Edwin A. Bergin <https://orcid.org/0000-0003-4179-6394>
 Ke Zhang <https://orcid.org/0000-0002-0661-7517>
 Kamber R. Schwarz <https://orcid.org/0000-0002-6429-9457>
 Colette Salyk <https://orcid.org/0000-0003-3682-6632>
 Arthur D. Bosman <https://orcid.org/0000-0003-4001-3589>

References

- Agúndez, M., Cernicharo, J., & Goicoechea, J. R. 2008, *A&A*, 483, 831
 Agúndez, M., Roueff, E., Le Petit, F., & Le Bourlot, J. 2018, *A&A*, 616, A19
 Alata, I., Cruz-Díaz, G. A., Muñoz Caro, G. M., & Dartois, E. 2014, *A&A*, 569, A119
 Alata, I., Jallat, A., Gavilan, L., et al. 2015, *A&A*, 584, A123
 Anderson, D. E., Bergin, E. A., Blake, G. A., et al. 2017, *ApJ*, 845, 13
 Anderson, D. E., Blake, G. A., Bergin, E. A., et al. 2019, *ApJ*, 881, 127
 Andrews, S. M., Wilner, D. J., Espaillat, C., et al. 2011, *ApJ*, 732, 42
 Astropy Collaboration, Robitaille, T. P., Tollerud, E. J., et al. 2013, *A&A*, 558, A33
 Banzatti, A., Pascucci, I., Bosman, A. D., et al. 2020, *ApJ*, 903, 124
 Bauer, I., Finocchi, F., Duschl, W. J., Gail, H.-P., & Schloeder, J. P. 1997, *A&A*, 317, 273
 Bergin, E. A., Blake, G. A., Ciesla, F., Hirschmann, M. M., & Li, J. 2015, *PNAS*, 112, 8965
 Bergin, E. A., Cleeves, L. I., Crockett, N., & Blake, G. A. 2014, *FaDi*, 168, 61
 Bergin, E. A., Cleeves, L. I., Gorti, U., et al. 2013, *Natur*, 493, 644
 Bethell, T. J., & Bergin, E. A. 2011a, *ApJ*, 740, 7
 Bethell, T. J., & Bergin, E. A. 2011b, *ApJ*, 739, 78
 Boogert, A. C. A., Gerakines, P. A., & Whittet, D. C. B. 2015, *ARA&A*, 53, 541
 Bosman, A. D., Bruderer, S., & van Dishoeck, E. F. 2017, *A&A*, 601, A36
 Bosman, A. D., Tielens, A. G. G. M., & van Dishoeck, E. F. 2018a, *A&A*, 611, A80
 Bosman, A. D., Walsh, C., & van Dishoeck, E. F. 2018b, *A&A*, 618, A182
 Bruderer, S. 2013, *A&A*, 559, A46
 Bruderer, S., Harsono, D., & van Dishoeck, E. F. 2015, *A&A*, 575, A94
 Carr, J. S., & Najita, J. R. 2008, *Sci*, 319, 1504
 Carr, J. S., & Najita, J. R. 2011, *ApJ*, 733, 102
 Chapillon, E., Guilloteau, S., Dutrey, A., & Piétu, V. 2008, *A&A*, 488, 565
 Ciesla, F. J., & Cuzzi, J. N. 2006, *Icar*, 181, 178
 Cleeves, L. I., Bergin, E. A., & Adams, F. C. 2014, *ApJ*, 794, 123
 Cleeves, L. I., Bergin, E. A., Qi, C., Adams, F. C., & Öberg, K. I. 2015, *ApJ*, 799, 204
 Cleeves, L. I., Öberg, K. I., Wilner, D. J., et al. 2018, *ApJ*, 865, 155
 Cridland, A. J., Bosman, A. D., & van Dishoeck, E. F. 2020, *A&A*, 635, A68
 Cridland, A. J., Pudritz, R. E., & Alessi, M. 2016, *MNRAS*, 461, 3274
 Draine, B. T., & Lee, H. M. 1984, *ApJ*, 285, 89
 Dullemond, C. P., & Dominik, C. 2004, *A&A*, 421, 1075
 Dutrey, A., Guilloteau, S., & Simon, M. 2003, *A&A*, 402, 1003
 Eistrup, C., Walsh, C., & van Dishoeck, E. F. 2016, *A&A*, 595, A83
 Eistrup, C., Walsh, C., & van Dishoeck, E. F. 2018, *A&A*, 613, A14
 Favre, C., Cleeves, L. I., Bergin, E. A., Qi, C., & Blake, G. A. 2013, *ApJL*, 776, L38
 Finocchi, F., Gail, H.-P., & Duschl, W. J. 1997, *A&A*, 325, 1264
 Fogel, J. K. J., Bethell, T. J., Bergin, E. A., Calvet, N., & Semenov, D. 2011, *ApJ*, 726, 29
 Furlan, E., Hartmann, L., Calvet, N., et al. 2006, *ApJS*, 165, 568
 Furuya, K., & Aikawa, Y. 2014, *ApJ*, 790, 97
 Gail, H.-P. 2001, *A&A*, 378, 192
 Gail, H.-P. 2002, *A&A*, 390, 253
 Gail, H.-P., & Tieloff, M. 2017, *A&A*, 606, A16
 Gibb, E. L., & Horne, D. 2013, *ApJL*, 776, L28
 Gordon, I. E., Rothman, L. S., Hill, C., et al. 2017, *JQSRT*, 203, 3
 Habing, H. J. 1968, *BAN*, 19, 421
 Harada, N., Herbst, E., & Wakelam, V. 2010, *ApJ*, 721, 1570
 Harries, T. J., Monnier, J. D., Symington, N. H., & Kurosawa, R. 2004, *MNRAS*, 350, 565
 Heays, A. N., Bosman, A. D., & van Dishoeck, E. F. 2017, *A&A*, 602, A105
 Hunter, J. D. 2007, *CSE*, 9, 90
 Krijt, S., Schwarz, K. R., Bergin, E. A., & Ciesla, F. J. 2018, *ApJ*, 864, 78
 Lee, J.-E., Bergin, E. A., & Nomura, H. 2010, *ApJL*, 710, L21
 Lynden-Bell, D., & Pringle, J. E. 1974, *MNRAS*, 168, 603
 Madhusudhan, N. 2019, *ARA&A*, 57, 617
 Mathis, J. S., Rumpl, W., & Nordisiek, K. H. 1977, *ApJ*, 217, 425
 McClure, M. K., Bergin, E. A., Cleeves, L. I., et al. 2016, *ApJ*, 831, 167
 McElroy, D., Walsh, C., Markwick, A. J., et al. 2013, *A&A*, 550, A36
 Meijerink, R., Pontoppidan, K. M., Blake, G. A., Poelman, D. R., & Dullemond, C. P. 2009, *ApJ*, 704, 1471
 Miotello, A., van Dishoeck, E. F., Williams, J. P., et al. 2017, *A&A*, 599, A113
 Mishra, A., & Li, A. 2015, *ApJ*, 809, 120
 Najita, J. R., Ádámkóvics, M., & Glassgold, A. E. 2011, *ApJ*, 743, 147
 Najita, J. R., Carr, J. S., Pontoppidan, K. M., et al. 2013, *ApJ*, 766, 134
 Öberg, K. I., Murray-Clay, R., & Bergin, E. A. 2011, *ApJL*, 743, L16
 Pascucci, I., Herczeg, G., Carr, J. S., & Bruderer, S. 2013, *ApJ*, 779, 178
 Pontoppidan, K. M., Salyk, C., Blake, G. A., et al. 2010, *ApJ*, 720, 887
 Price, E. M., Cleeves, L. I., & Öberg, K. I. 2020, *ApJ*, 890, 154
 Price-Whelan, A. M., Sipőcz, B. M., Günther, H. M., et al. 2018, *AJ*, 156, 123

- Reback, J., McKinney, W., Mendel, B., et al. 2021, pandas-dev/pandas: Pandas 1.2.2 v.0.25.1, Zenodo, doi:[10.5281/zenodo.3509134](https://doi.org/10.5281/zenodo.3509134)
- Reboussin, L., Wakelam, V., Guilloteau, S., Hersant, F., & Dutrey, A. 2015, *A&A*, **579**, A82
- Salyk, C. 2020, slabspec, v1.0, Zenodo, [10.5281/zenodo.4037306](https://doi.org/10.5281/zenodo.4037306)
- Salyk, C., Pontoppidan, K. M., Blake, G. A., Najita, J. R., & Carr, J. S. 2011, *ApJ*, **731**, 130
- Savage, B. D., & Sembach, K. R. 1996, *ARA&A*, **34**, 279
- Schwarz, K. R., Bergin, E. A., Cleeves, L. I., et al. 2016, *ApJ*, **823**, 91
- Schwarz, K. R., Bergin, E. A., Cleeves, L. I., et al. 2018, *ApJ*, **856**, 85
- Tange, O. 2018, GNU Parallel 2018, Zenodo, doi:[10.5281/zenodo.1146014](https://doi.org/10.5281/zenodo.1146014)
- Teague, R., Bae, J., & Bergin, E. A. 2019, *Natur*, **574**, 378
- van der Walt, S., Colbert, S. C., & Varoquaux, G. 2011, *CSE*, **13**, 22
- van't Hoff, M. L. R., Bergin, E. A., Jørgensen, J. K., & Blake, G. A. 2020, *ApJL*, **897**, L38
- Walsh, C., Nomura, H., & van Dishoeck, E. 2015, *A&A*, **582**, A88
- Wei, C.-E., Nomura, H., Lee, J.-E., et al. 2019, *ApJ*, **870**, 129
- Wells, M., Pel, J. W., Glasse, A., et al. 2015, *PASP*, **127**, 646
- Woitke, P., Min, M., Thi, W. F., et al. 2018, *A&A*, **618**, A57
- Yu, M., Willacy, K., Dodson-Robinson, S. E., Turner, N. J., & Evans, N. J., II 2016, *ApJ*, **822**, 53
- Zhang, K., Bergin, E. A., Blake, G. A., Cleeves, L. I., & Schwarz, K. R. 2017, *NatAs*, **1**, 0130
- Zhang, K., Bergin, E. A., Schwarz, K., Krijt, S., & Ciesla, F. 2019, *ApJ*, **883**, 98
- Zhang, K., Bosman, A. D., & Bergin, E. A. 2020, *ApJL*, **891**, L16